Directional wavelet analysis on the sphere: Application to gravity and topography of the terrestrial planets

Pascal Audet[1]

Received 6 August 2010; revised 25 October 2010; accepted 5 November 2010; published 8 January 2011.

[1] The spectral relations (admittance and correlation) between gravity and topography are often used to obtain information on the density structure, flexural support, and heat flow of planetary lithospheres. Mapping spatial variations in these quantities requires spatiospectral analysis techniques. Here we describe the application of a directional, continuous spherical wavelet transform using a wavelet basis constructed from the superposition of azimuthally adjacent complex Morlet wavelets, in a manner similar to the "fan" wavelet developed in the plane. The method is applied to gravity and topography of the Earth, Venus, Mars, and the Moon. The wavelet coefficients are used to compute isotropic and directional wavelet autospectra and cross spectra, which are then combined to form the admittance and correlation functions. The resulting maps offer insights into lithospheric structure of the terrestrial planets. In particular we show that the Earth and Venus have uniformly low positive admittance and high correlation, whereas Mars and the Moon display hemispherical contrasts with large negative and anisotropic coefficients coinciding with lowlands. As has long been known, the two largest impact basins in the inner solar system, the South Pole–Aitken basin on the Moon and the Hellas basin on Mars, display low positive admittance and high correlation, indicating isostatic compensation. In contrast, most other impact basins, particularly the Martian and lunar mascons, show negative coefficients at low wavelet degrees suggesting flexural support by a strong lithosphere. These results imply that, although simple isotropic flexural models can account for most observations, future models may need to incorporate anisotropy as an additional parameter.

Citation: Audet, P. (2011), Directional wavelet analysis on the sphere: Application to gravity and topography of the terrestrial planets, *J. Geophys. Res.*, *116*, E01003, doi:10.1029/2010JE003710.

1. Introduction

[2] The analysis of gravity and topography data is often the only source of information on the structure of the crust and mantle of terrestrial planets [*Phillips and Lambeck*, 1980; *Wieczorek*, 2007]. In particular, their cross analysis (admittance and correlation) provides valuable information on the flexural support of planetary lithospheres and by inference on surface heat flow [e.g., *Solomon and Head*, 1990; *Simons et al.*, 1997; *Zuber et al.*, 2000; *Arkani-Hamed*, 2000; *McKenzie et al.*, 2002; *McGovern et al.*, 2002; *Belleguic et al.*, 2005]. Gravity (g) and topography (h) data are normally given in terms of spherical harmonics, which are the natural orthogonal basis for global functions defined on the sphere. The admittance (Z) and correlation (γ) are functions of the spherical harmonic degree l and are defined as the ratio of the cross-spectrum S_{gh} of g and h to individual spectra S_{gg} and S_{hh},

$$Z(l) = \frac{S_{gh}(l)}{S_{hh}(l)} \tag{1}$$

and

$$\gamma(l) = \frac{S_{gh}(l)}{\sqrt{S_{gg}(l)\, S_{hh}(l)}}. \tag{2}$$

[3] These quantities can be inverted using a thin elastic shell equation for the flexural support of transverse surface and internal loads to estimate the density structure and the thickness T_e of an effectively elastic lithosphere [e.g., *Turcotte et al.*, 1981; *McGovern et al.*, 2002; *Belleguic et al.*, 2005]. The elastic shell is characterized by a flexural wavelength λ_F which depends on the loading structure, rigidity and density [*Turcotte et al.*, 1981]. Generally speaking, at short wavelengths ($\lambda \ll \lambda_F$) the loads are supported by elastic stresses; at longer wavelengths ($\lambda \gg \lambda_F$) the loads are fully compensated by deflection of the shell. Mapping variations in T_e is thus an intrinsically involved

[1]Department of Earth and Planetary Science, University of California, Berkeley, California, USA.

Copyright 2011 by the American Geophysical Union.
0148-0227/11/2010JE003710

spatiospectral problem that requires simultaneous spatial and spectral localization techniques to calculate equations (1) and (2). Although rarely used, the anisotropy in the admittance and correlation provides an additional constraint on the flexural support of surface and internal loads [*Lowry and Smith*, 1995; *Simons et al.*, 2000, 2003; *Kirby and Swain*, 2006; *Audet and Mareschal*, 2007; *Audet et al.*, 2007]. In particular, it may provide important information on the directionality in loading structure and therefore on lithosphere fabric.

[4] Several methods have been developed to estimate spatial and directional variations in T_e on Cartesian, two-dimensional grids [see *Audet and Mareschal*, 2007]. These include the maximum entropy [*Lowry and Smith*, 1994], multitaper [*Simons et al.*, 2000; *Pérez-Gussinyé et al.*, 2004] and wavelet transform [*Kirby and Swain*, 2006; *Audet and Mareschal*, 2007] methods. On the sphere, recent developments include the work by *Simons et al.* [1997] who designed a moving window technique using spherical caps similar to a Welch periodogram method. *Wieczorek and Simons* [2005] and *Simons et al.* [2006] further improved the windowing approach by designing a multitaper analysis on the sphere from the maximization of energy within a spherical window. A pseudowavelet analysis was constructed by *Kido et al.* [2003] using an azimuthally averaged Gabor function corrected for spherical geometry. All of the above techniques developed on the sphere calculate isotropic estimates; that is, directional information is averaged out, hampering the detection of anisotropy in the data.

[5] A number of attempts have been made to extend the 2-D wavelet transform to the unit sphere (see *Antoine et al.* [2004] for a review). Using a group-theoretical approach, *Antoine and Vandergheynst* [1999] constructed a framework for wavelets defined on the sphere which satisfy a number of natural requirements. The algorithm requires the calculation of a spherical convolution at each wavelet scale which is a very expensive numerical operation. Recently a fast, directional, continuous wavelet transform on the sphere was implemented by *McEwen et al.* [2007a]. The algorithm was applied to the local and directional analysis of the cosmic microwave background radiation in cosmology using real-valued wavelets (Mexican Hat, Butterfly, real Morlet) [*McEwen et al.*, 2005, 2007b]. Here we describe the application of the continuous wavelet transform using a complex directional wavelet on the sphere, constructed from the superposition of azimuthally adjacent complex Morlet wavelets, similar to the Euclidian "fan" wavelet [*Kirby*, 2005]. Finally, we apply the technique to the gravity and topography of Earth, Venus, Mars and the Moon and discuss the implications for the flexural support of the lithosphere.

2. Continuous Spherical Wavelet Transform

[6] In this section we discuss the implementation of the continuous spherical wavelet transform (CSWT) as described by *McEwen et al.* [2007a].

2.1. Wavelet Transform

[7] The CSWT is defined by extending the Euclidian analysis to spherical geometry using the correspondence principle. In this approach a stereographic projection is used to define affine transformations (linear transformations and translations) on the unit sphere and map Euclidian wavelets into their spherical equivalents [*Wiaux et al.*, 2005]. The stereographic projection is the unique unitary, radial and conformal diffeomorphism between the sphere and the plane (i.e., a smooth, invertible function that maps one differentiable manifold to another). It is thus chosen to construct a correspondence between wavelets on the plane ($\mathbb{R}^2$) and the 2-sphere (S^2) [*Wiaux et al.*, 2005]. This operation is defined by projecting a point on the unit sphere to a point on the plane defined by the tangent at the north pole, and casting a ray through the point and the south pole (Figure 1). The point on the unit sphere is mapped onto the intersection of the ray and the tangent plane.

[8] The natural extension of Euclidian translations on the unit sphere are rotations, characterized by the elements of the rotation group SO(3) (i.e., the Special Orthogonal Group in $\mathbb{R}^3$), where a rotation about the origin may be expressed as the product of two rotations about the z axis ($\mathcal{R}_z$), and one about the y axis ($\mathcal{R}_y$),

$$\mathcal{R}_z(A) = \begin{pmatrix} \cos(A) & -\sin(A) & 0 \\ \sin(A) & \cos(A) & 0 \\ 0 & 0 & 1 \end{pmatrix}$$
$$\mathcal{R}_y(A) = \begin{pmatrix} \cos(A) & 0 & \sin(A) \\ 0 & 1 & 0 \\ -\sin(A) & 0 & \cos(A) \end{pmatrix} \tag{3}$$

and is defined by

$$\mathcal{R}_\rho \equiv \mathcal{R}_z(\alpha)\mathcal{R}_y(\beta)\mathcal{R}_z(\gamma), \tag{4}$$

where $0 \le \alpha,\gamma < 2\pi$ and $0 \le \beta < \pi$ are the Euler angles and $(\alpha,\beta,\gamma) \equiv \rho \in \mathrm{SO}(3)$. The rotation of a square-integrable function f on S^2 (i.e., $f \in L^2(S^2)$) is therefore given by

$$\left(\mathcal{R}_\rho f\right)(\omega) = f\left(\rho^{-1}\omega\right),\ \rho \in \mathrm{SO}(3), \tag{5}$$

where $\omega \equiv (\theta,\phi) \in S^2$ denotes the colatitude and longitude of a spherical coordinate system.

[9] Dilations on the unit sphere are constructed by first lifting the sphere to the plane by the stereographic projection, performing the Euclidian dilation in the plane, and back projecting the Euclidian dilation onto the sphere. A spherical dilation is thus defined by

$$\left(\mathcal{D}_a f\right)(\omega) = f_a(\omega) = \sqrt{\lambda(a,\theta)} f\left(\omega_{1/a}\right),\ a \in \mathbb{R}_*^+, \tag{6}$$

where $\omega_a = (\theta_a,\phi)$ and $\tan(\theta_a/2) = a\tan(\theta/2)$. The $\lambda(a,\theta)$ cocycle term is introduced to preserve the 2-norm and is given by

$$\lambda(a,\theta) = \frac{4a^2}{\left[(a^2-1)\cos\theta + (a^2+1)\right]^2}. \tag{7}$$

[10] The wavelet dilation a can take any admissible value determined by the resolution of the data. An overcomplete wavelet basis on the sphere may be constructed by rotations and dilations of an admissible mother spherical wavelet $\psi \in L^2(S^2)$. The wavelet basis functions $\psi_{a,\rho}$ are

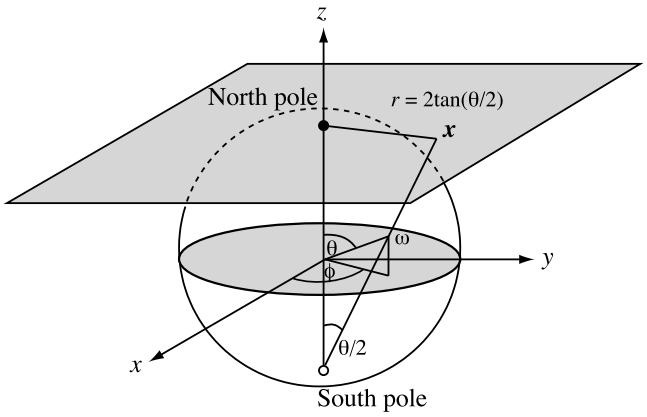

Figure 1. Stereographic projection of the sphere onto the plane (modified from *McEwen et al.* [2007a] (©2006 IEEE)). A vector **x** is mapped onto the sphere at a point *w* and vice versa.

thus given by the product of both operators $\mathcal{R}\rho$ and $\mathcal{D}_a$ on the mother wavelet $\psi_{a,\rho} = \mathcal{R}_\rho\, \mathcal{D}_a\, \psi$, $\rho \in \mathrm{SO}(3)$, $a \in \mathbb{R}^+_*$.

[11] Mother spherical wavelets are constructed by projecting admissible Euclidian planar wavelets onto the sphere by an inverse stereographic projection,

$$\psi_{S^2}(\theta,\phi) = \frac{2}{1+\cos\theta}\,\psi_{\mathbb{R}^2}(r,\phi), \tag{8}$$

where $r = \tan(\theta/2)$. The modulating term is again introduced to preserve the 2-norm.

[12] Finally, the CSWT of $f \in L^2(S^2)$ is given by the projection onto each wavelet basis function,

$$W(a,\rho) = \int_{S^2} \psi^*_{a,\rho}(\omega)\, f(\omega)\; d\omega, \tag{9}$$

where the asterisk (*) denotes complex conjugation and $d\omega \equiv \sin\theta\, d\theta\, d\phi$. All orientations in the rotation group SO(3) are considered; directional structure is thus naturally incorporated. It is important to note, however, that only local directions make any sense on the 2-sphere; there will always be a singular point where the definition fails [*McEwen et al.*, 2007a]. We note that although the CSWT can be defined using anisotropic dilations to probe directionality in the data, the wavelets are not admissible in this case and their use is not advocated here [*McEwen et al.*, 2007a].

2.2. Spherical Morlet Wavelet and Relatives

[13] The choice of a suitable mother wavelet depends on the nature of the underlying process analyzed, the need for real or complex-valued basis functions and ultimately on their ability to detect oriented features. Estimation of the flexural support from gravity and topography data requires the solution of a harmonic equation on the sphere [e.g., *Turcotte et al.*, 1981]. The natural basis in this case is a wavelet constructed from a harmonic function modulated by a localizing window. One such wavelet is the Morlet wavelet, which also possesses a natural property of directional selectivity on the plane, allowing the detection of oriented features.

[14] The Morlet wavelet in $\mathbb{R}^2$ is defined by a complex exponential modulated by a Gaussian function,

$$\psi_{\mathbb{R}^2}(\mathbf{x}) = \exp(i\,\mathbf{k}_0\cdot\mathbf{x})\exp\left(\frac{-\,\|\,\mathbf{x}\,\|^2}{2}\right), \tag{10}$$

where $\mathbf{k}_0 = (k_0,0)^T$ is the wave vector of the underlying harmonic function. The Morlet wavelet is a complex-valued function that yields phase information in the direction of the wave vector. In this version the Morlet wavelet is not strictly admissible unless k_0 is very large. However, for $k_0 \approx 5$, the error introduced is small (10^{-5}) and can be neglected [*Kirby*, 2005]. The Fourier transform of the Euclidian Morlet wavelet is a Gaussian function centered on the wave vector $\mathbf{k}_0$ and thus constitutes a bandpass filter. The spherical Morlet wavelet is constructed by the stereographic projection of the Euclidian Morlet wavelet onto the sphere. The effective size on the sphere of the internal structure of the Morlet wavelet is defined as the angular separation between the first zero crossings in the direction of the wave vector and is given by

$$\xi(a) \approx \frac{a\pi}{k_0}. \tag{11}$$

[15] The dilation a is related to an equivalent spherical harmonic degree l_a via

$$a = \frac{k_0}{\sqrt{l_a(l_a+1)}}, \tag{12}$$

which in turn can be related to a spatial wavelength

$$\lambda \approx \frac{2\pi}{l_a}R, \tag{13}$$

where R is the planet's mean radius.

[16] Because wavelets have a finite bandwidth, wavelet coefficients at a given dilation (or degree l_a) include information from neighboring spherical harmonic degrees. In the remainder of this paper we will refer to l_a as the *wavelet degree*. In practice, although the dilation a can take any arbitrary positive real value ($a \in \mathbb{R}^+_*$), we select dilations a for which l_a s are nonzero integers.

[17] The Morlet wavelet is a directional filter and captures information in the direction of the wave vector. Rotation of the Morlet wavelet along different azimuths is performed by the rotation operator over the Euler angle γ (Figures 2a and 2d). An isotropic wavelet can also be constructed by averaging daughter spherical Morlet wavelets $\psi^M_{a,\rho}$ over all rotations of the angle $\gamma \in [0,\pi)$,

$$\psi^I_{a,\rho_{\langle\gamma\rangle}}(\omega) = \frac{1}{N_\gamma}\sum_\gamma \left(\mathcal{R}_{\rho|_\gamma}\psi^M_{a,\rho}\right)(\omega), \tag{14}$$

where the rotation operator $\mathcal{R}_{\rho|\gamma}$ indicates rotation over γ only and $\rho_{\langle\gamma\rangle} = (\alpha,\beta)$ (Figures 2c and 2f). This is the spherical equivalent of the Euclidian "isotropic" fan wavelet (hence the subscript "I"), thus named for its shape in the wave vector domain [*Kirby*, 2005].

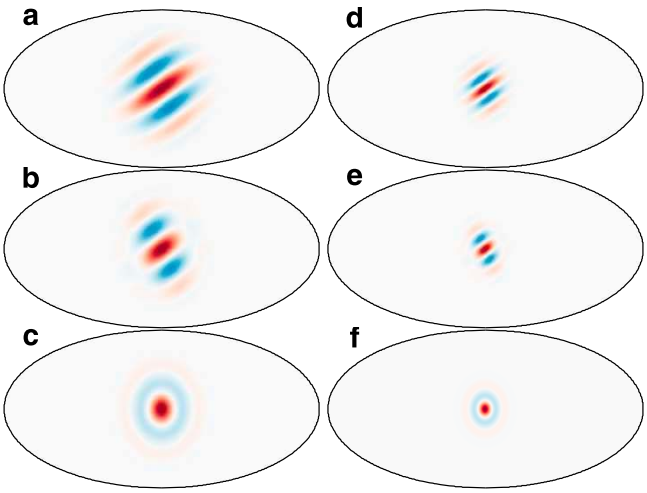

Figure 2. Spherical Morlet and fan wavelets used in this study. (a) Real Morlet wavelet at $l_a = 8$ oriented 150°. (b) Real directional fan wavelet at $l_a = 8$ oriented 150° calculated from the superposition of 6 Morlet wavelets with azimuthal separation of 15°. (c) Real isotropic fan wavelet at $l_a = 8$ calculated from the superposition of 12 Morlet wavelets. (d–f) Same as Figures 2a–2c but for $l_a = 16$. For all cases, $k_0 = 5.336$.

[18] By restricting the rotations over a smaller range $N_{\gamma'} < N_\gamma$, the fan wavelet can retrieve directional information,

$$\psi^D_{a,\rho'}(\omega) = \frac{1}{N_{\gamma'}} \sum_{\gamma} \left(\mathcal{R}_{\rho|_\gamma} \psi^M_{a,\rho} \right)(\omega), \tag{15}$$

where $\rho' = (\alpha,\beta,\gamma')$. Equation (15) thus describes a "directional" fan wavelet (subscript "D"; Figures 2b and 2e). We note at this point that the different versions of the fan wavelet are never used as described by equations (14) and (15). The averaging is instead performed on the wavelet coefficients (or product thereof) obtained from discrete directional spherical Morlet wavelets,

$$W^I(a, \rho_{\langle\gamma\rangle}) = \frac{1}{N_\gamma} \sum_{\gamma} \left(\mathcal{R}_{\rho|_\gamma} W(a,\rho) \right), \tag{16}$$

and

$$W^D(a, \rho') = \frac{1}{N_{\gamma'}} \sum_{\gamma} \left(\mathcal{R}_{\rho|_\gamma} W(a,\rho) \right). \tag{17}$$

2.3. Cross-Spectral Analysis

[19] Equation (9) is used to compute a wavelet scalogram, which represents the energy of a signal f at a given wavelet dilation a and rotation $\rho \in \mathrm{SO}(3)$,

$$S_{ff}(a,\rho) = \langle W_f(a,\rho)\, W_f^*(a,\rho) \rangle, \tag{18}$$

where the brackets $\langle\ \rangle$ denote some kind of averaging. A natural choice is to perform averaging of the product of wavelet coefficients over rotations of the Euler angle γ, as in the fan averaging, to obtain isotropic estimates

$$S_{ff}(a, \rho_{\langle\gamma\rangle}) = \frac{1}{N_\gamma} \sum_{\gamma} \left[\mathcal{R}_{\rho|\gamma} \left(W_f(a,\rho)\, W_f^*(a,\rho) \right) \right], \tag{19}$$

or directional estimates

$$S_{ff}(a, \rho') = \frac{1}{N_{\gamma'}} \sum_{\gamma} \left[\mathcal{R}_{\rho|_\gamma} \left(W_f(a,\rho)\, W_f^*(a,\rho) \right) \right]. \tag{20}$$

[20] The wavelet cross scalogram of 2 functions $f,g \in L^2(S^2)$ is defined as

$$S_{fg}(a,\rho) = \langle W_f(a,\rho)\, W_g^*(a,\rho) \rangle, \tag{21}$$

and averaging can be performed either as in equation (19) or (20).

[21] The wavelet scalograms and cross scalograms are combined to compute the wavelet admittance

$$Z_{fg}(a,\rho) = \frac{\Re\left[S_{fg}(a,\rho)\right]}{S_{gg}(a,\rho)}, \tag{22}$$

and correlation

$$\gamma_{fg}(a,\rho) = \frac{\Re\left[S_{fg}(a,\rho)\right]}{\sqrt{S_{gg}(a,\rho)\, S_{ff}(a,\rho)}}, \tag{23}$$

where the symbol $\Re$ denotes taking the real component of the cross scalogram. We note that one could calculate an imaginary admittance and correlation by taking the imaginary part of the cross scalogram, which has been shown to influence the validity of the linear isostatic model described in section 4 [*Kirby and Swain*, 2009].

2.4. Caveats

[22] The spatiospectral localization of the Morlet wavelet is entirely controlled by the wave number k_0. Wavelets with large values of k_0 are better localized in spectral space and peak at degrees close to the theoretical value l_a; wavelets with low values of k_0 are better localized in physical space, however they peak at degrees larger than the theoretical l_a. This is shown in Figure 3 where the spectral peaks have a width inversely proportional to k_0 and are displaced toward larger degrees with respect to the theoretical l_a.

[23] Another notable effect shown in Figure 3 is the breakdown of admissibility for wavelets with $l_a < k_0$. This effect is shown by the departure from a Gaussian shape and lower RMS amplitude where $l_a < k_0$. To ensure admissibility and maintain good spatial localization we select $k_0 = 5.336$ [*Kirby*, 2005] and limit the analysis to wavelet degrees $l_a \geq 6$.

2.5. Algorithm

[24] Spherical convolutions on a sphere require the use of a particular tessellation. We use the HEALPix tessellation which is an equal area pixelization scheme [*Górski et al.*, 2005]. We proceed by first transforming the spherical harmonic models of gravity and topography to the spherical

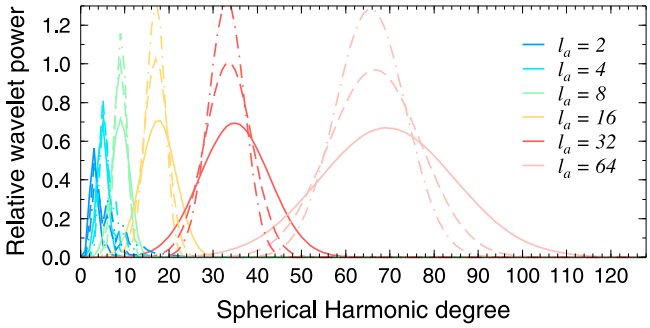

Figure 3. Wavelet power spectra at various wavelet degrees l_a using different values of the Morlet wave number k_0. Solid lines, k_0 = 4; dashed lines, k_0 = 6; dash-dotted lines, k_0 = 8. Each set of power spectra at a given k_0 is normalized to the maximum value obtained with k_0 = 6.

coordinate system on a 30 arc min grid, and secondly by mapping the grids onto a HEALPix grid with resolution N_{side} = 128, which corresponds to a total number of pixels of $N_{pix} = 12 \times N_{side}^2$ = 196,608. The grids are then used as inputs into the software FastCSWT which calculates the spherical convolution at each dilation and azimuth previously defined [*McEwen et al.*, 2007a]. The wavelet coefficients can be averaged using equations (16) and (17) to obtain isotropic and directional quantities. Alternatively we can calculate the scalograms and cross scalograms by averaging the product of wavelet coefficients using equations (19) or (20). From these quantities we then form the admittance and correlation functions using equations (22) and (23).

[25] In this work we discretize the azimuth range into 24 equally spaced intervals over the range $[0,2\pi)$ with a spacing of 15°. The isotropic fan averaging is performed over the first 12 azimuthal samples because the remaining 12 coefficients contain redundant information. The directional fan averaging is performed over 6 coefficients, effectively averaging over 90°, spaced at every 15° intervals up to 180°.

[26] The directional wavelet coefficients are functions of 4 variables (equation (9)): 1 for dilation, 2 for location and 1 for azimuth. At each given dilation and location, the wavelet coefficients are thus function of azimuth. We define a measure of directional variability (or anisotropy) by fitting a cosine function to the azimuthal variations using a least squares algorithm. The amplitude and phase of the fitted cosine function can then be represented as a vector quantity, where the phase corresponds to the azimuth where coefficients are largest (or least negative), and the amplitude defines the anisotropic magnitude and is always positive. In this paper we only report spatial variations in the anisotropic magnitude at each dilation, which allows us to plot the directional variability as color contours in a way similar to the isotropic estimates (see section 3). We note that this representation is useful for purely visual purposes, whereas a formal inversion of wavelet coefficients would require using the full range of parameters.

3. Application to Gravity and Topography of Terrestrial Planets

[27] In this section we describe the application of the wavelet transform to the gravity and topography of Earth, Venus, Mars and the Moon. The spectral resolution and truncation of each data set used in the wavelet analysis are summarized in Table 1. We use the radial gravity anomaly calculated by subtracting the J_2 term from the gravitational potential to account for the hydrostatic flattening contribution, and refer to it simply as *gravity*.

3.1. Earth

3.1.1. Data

[28] We use Earth's global topographic model from the 1 arc minute resolution ETOPO1 [*Amante and Eakins*, 2009] (Figure 4a). Elevation is referenced above the EGM96 geoid model. The topography model is a combination of several regional and global data sets. The main uncertainties in the bathymetry originate from estimates calculated from marine gravity data [*Sandwell and Smith*, 1997; *Smith and Sandwell*, 1997]. This caveat limits the use of admittance and correlation functions over the oceans at short wavelengths. The gravitational model is taken from the EGM2008 model (Figure 4b).

3.1.2. Wavelet Transform

[29] Isotropic wavelet coefficients of gravity and topography are shown in Figure 4c for a range of wavelet degrees. At low degrees, large positive coefficients of topography are associated with continental areas, whereas negative coefficients coincide with ocean basins, as expected. Wavelet coefficients at increasing wavelet degrees outline the continental margins where topographic gradients are largest. Wavelet coefficients of gravity generally follow the same trends, although differences are observed at the lowest degrees. Such differences are attributed to large-scale, sublithospheric structure induced by a combination of convection processes, isostatic glacial rebound signals, etc. [*Simons and Hager*, 1997].

[30] Figure 4d shows the magnitude of the anisotropic wavelet coefficients. Large values indicate significant directional variability in the coefficients, whereas low values show that coefficients do not vary much with azimuth (i.e., directionally invariant, or isotropic). At low degrees the largest directional variations in topography are distributed mostly over continental areas and margins, whereas the variations in gravity do not correlate with topographic features, similar to the isotropic coefficient maps. We note that the largest anisotropic coefficients of gravity are better correlated with large-scale upwellings and downwellings inferred from gravity and seismic tomography data [e.g., *Spasojevic et al.*, 2010]. At larger wavelet degrees both the topography and gravity coefficients outline the continents and major topographic features.

3.1.3. Wavelet Admittance and Correlation

[31] Maps of isotropic wavelet admittance and correlation are shown in Figure 5a. There are two main features found in the admittance maps: (1) wavelet admittance at low degrees is uniformly low and (2) admittance increases in continental areas at large wavelet degrees and remains low over ocean basins. The correlation maps show elevated values at large wavelet degrees. At low degrees, negative values reflect deep convection processes that are anticorrelated with topography. We note that only a few localized regions (e.g., southeastern United States, Amazonian basin) exhibit negative admittance and correlation in continental areas.

Table 1. Spectral Resolution of Gravity (G) and Topography (H) Data for Each Planetary Body[a]

Planet	Radius (km)	l_{trunc} (λ in km)	$l^G_{\max}$ (λ in km)	$l^H_{\max}$ (λ in km)
Earth	6371	128 (313)	2159 (19)	~21640 (1.85)
Venus	6051	65 (585)	180 (211)	360 (106)
Mars	3389	90 (237)	110 (194)	90 (237)
Moon	1737	100 (109)	100 (109)	360 (30)

[a]Here l_{trunc} is the degree (and order) at which models are truncated for the wavelet analysis. Here $l_{\max}$ is the largest degree (and order) resolved for each model. Smallest equivalent wavelengths calculated from equation (13) are shown in parentheses.

[32] Figure 5b shows the magnitude of the anisotropic wavelet coefficients of admittance and correlation. Similar features are observed in the admittance maps: (1) uniformly low anisotropic coefficients at low wavelet degrees and (2) larger coefficients over continents at larger wavelet degrees. The anisotropy in the correlation maps is quite large over some areas but does not coincide with topographic features.

3.2. Venus

3.2.1. Data

[33] Gravity and topography of Venus were measured by the orbiting spacecraft Magellan between 1990 and 1994. We use the spherical harmonic models SHTJV360u (topography) and SHGJ180u (gravity) (Figures 6a and 6b). Due to the elliptical orbit of the spacecraft, resolution and error is highly variable on the surface of the planet. Errors are larger for nonsectoral terms ($|m| \neq l$) which can affect directional estimates of the wavelet transform. To mitigate these effects the models are truncated at degree and order 65, which implies that the wavelet coefficients are inaccurate for wavelet degrees $l_a > 32$ (Figure 3).

3.2.2. Wavelet Transform

[34] Isotropic wavelet coefficients of gravity and topography are shown in Figure 6c. The largest signals at low wavelet degrees are associated with high topography (Ishtar and Aphrodite Terrae) and the Beta Regio volcanic edifice.

[35] Anisotropic wavelet coefficients of gravity and topography are shown in Figure 6d. At low wavelet degrees the anisotropic signature is dominated by the region around Beta Regio and high topography in the Terrae. As wavelet degree increases, the anisotropic signal is maximum in the interior of elevated plateaux, whereas the low-elevation plains remain isotropic.

3.2.3. Wavelet Admittance and Correlation

[36] The wavelet admittance and correlation maps are shown in Figure 7a. The admittance and correlation do not change significantly over the portion of wavelet degrees analyzed. The admittance is slightly larger than Earth's admittance, perhaps indicating the different nature of convection on Venus. Interestingly, the correlation remains

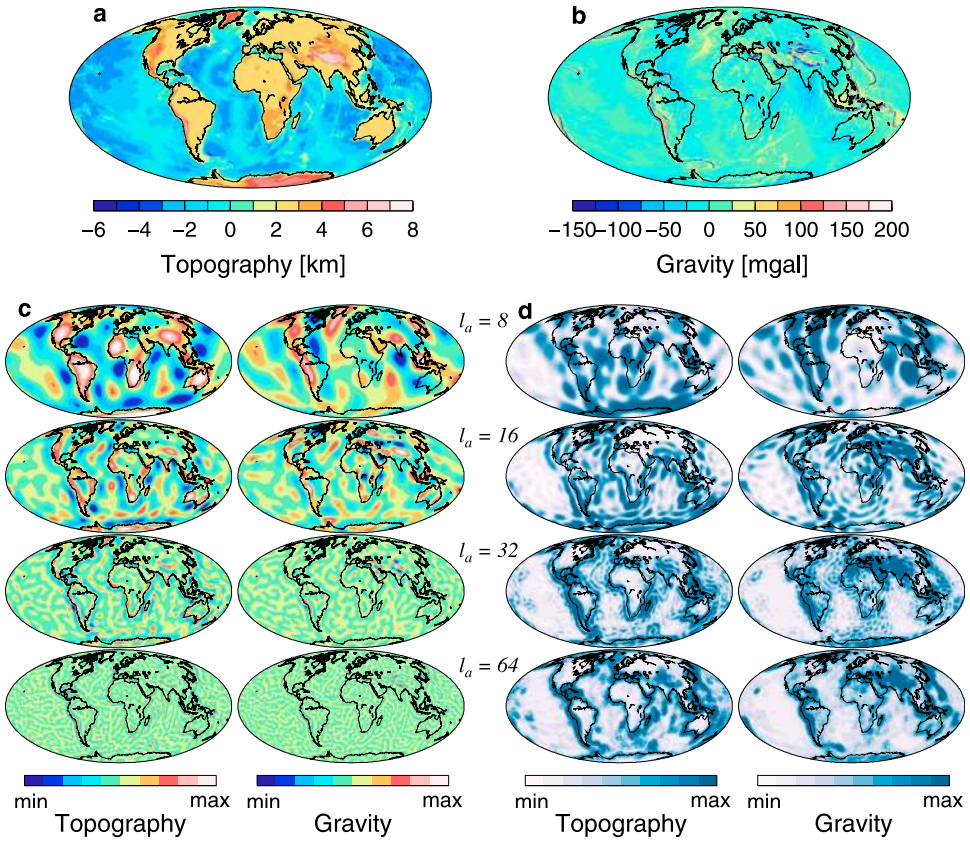

Figure 4. (a) Topography and (b) gravity of the Earth are decomposed into (c) isotropic and (d) anisotropic wavelet coefficients as a function of spherical wavelet degree l_a using a real Morlet wavelet. The colors are scaled to the minimum and maximum values in each plot for clarity.

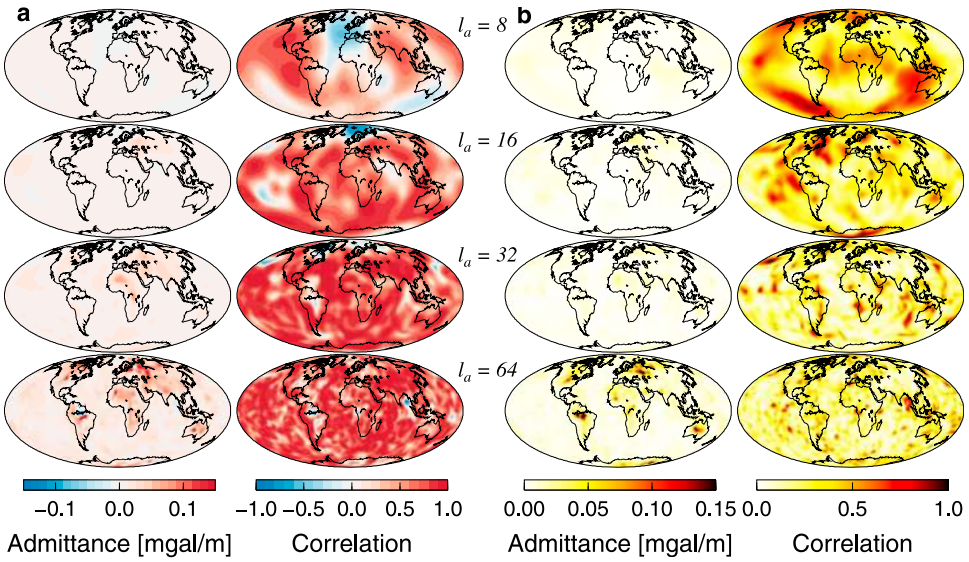

Figure 5. (a) Isotropic and (b) anisotropic wavelet (left) admittance and (right) correlation of the Earth as a function of wavelet degree l_a.

everywhere positive even for the lowest degrees, suggesting a more homogeneous sublithospheric mantle compared to Earth. The large Terrae generally show lower admittance, whereas regions of higher admittance are located in the various low-elevation plains and around the Beta Regio volcanic rise. Correlation degrades at wavelet degree 64, however this is likely an effect of the loss of fidelity with the gravity model at such wavelengths, and the truncation of the spherical harmonic model at degree 65.

[37] Figure 7b shows the anisotropic wavelet coefficients of admittance and correlation. Both the admittance and correlation show little anisotropy. Anisotropic correlation is

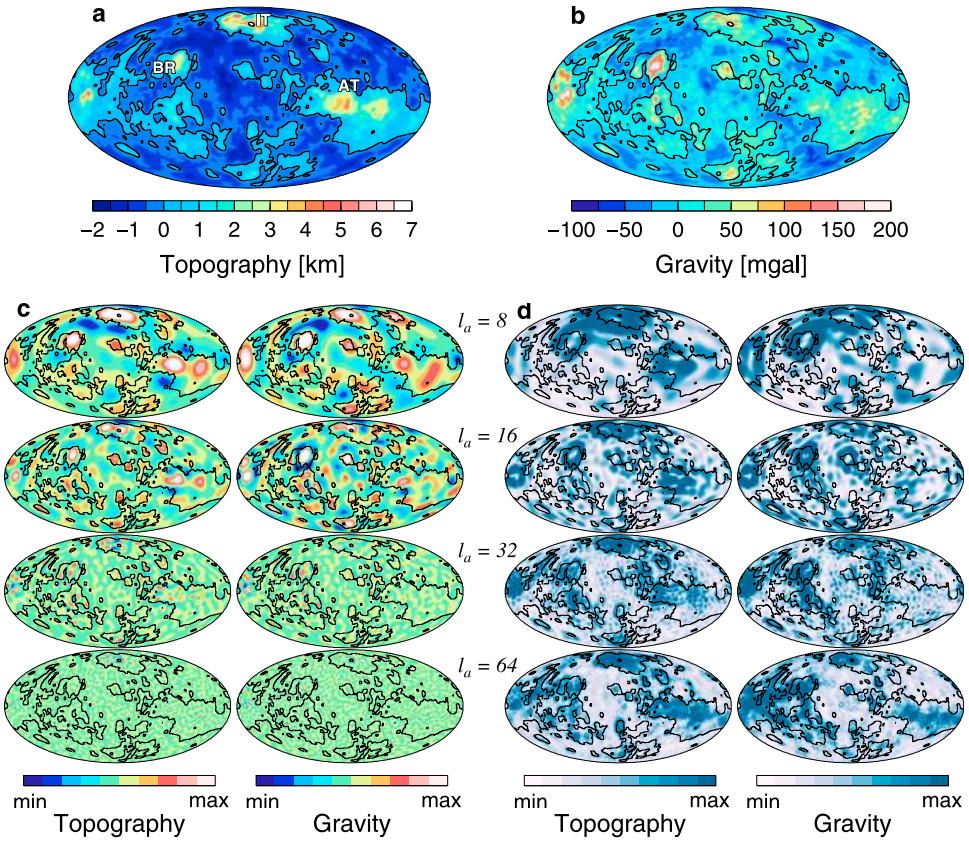

Figure 6. Same as Figure 4 but for Venus. AT, Aphrodite Terra; BR, Beta Regio; IT, Ishtar Terra.

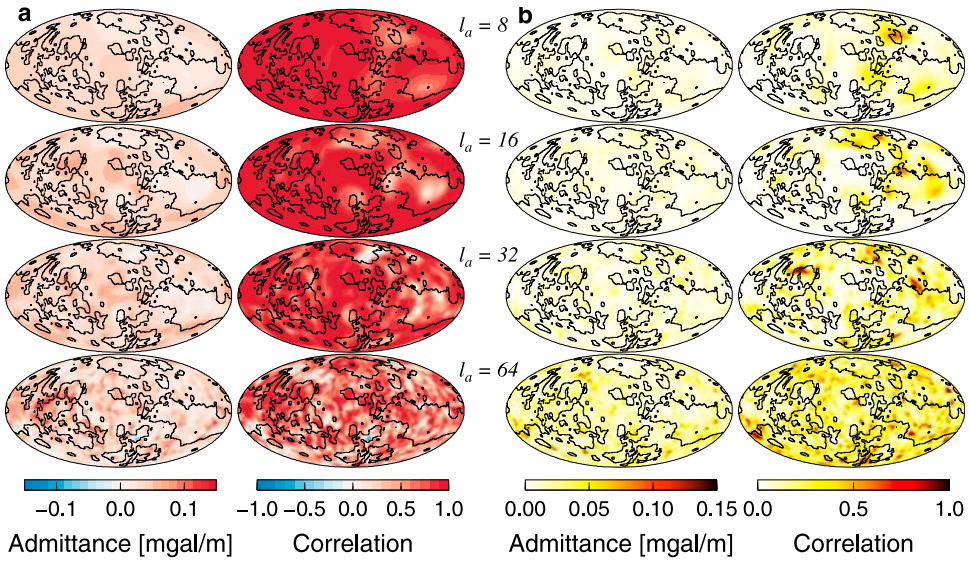

Figure 7. Same as Figure 5 but for Venus.

maximum around the Aphrodite and Ishtar Terrae. Larger anisotropic coefficients at wavelet degree 64 may also reflect associated errors for nonsectoral spherical harmonic coefficients, which produce strong azimuthal artifacts.

3.2.4. Comparison With Previous Studies

[38] The spatiospectral localization technique of *Simons et al.* [1997] was first applied to study gravity and topography on Venus. In their study they calculated geoid-to-topography ratios globally and interpreted their results at a number of locations, mostly around identified topographic features. Their global maps of admittance (Figure 13 of *Simons et al.* [1997]) at spherical harmonic degrees 8 and 16 can be directly compared to our results (Figure 7a). Despite differences in localization properties of the wavelet and windowing kernels, the results are in general agreement, showing high positive admittance over the volcanic edifices and lower admittance for the high-elevation Terrae.

3.3. Mars

3.3.1. Data

[39] The Martian topographic model is obtained form the Mars Orbiter Laser Altimeter (MOLA) instrument aboard the Mars Global Surveyor (MGS) mission [*Smith et al.*, 1999b]. We use the GTM090 model, which gives absolute radius from Mars' center of mass, or shape. The radial gravitational model JGMRO_110b2 is obtained by radio tracking of the Mars Reconnaissance Orbiter (MRO) mission [*Smith et al.*, 1999a] (Figure 8b). The Martian topography is calculated by removing the areoid contribution to the shape model [*McGovern et al.*, 2002] (Figure 8a).

3.3.2. Wavelet Transform

[40] The isotropic wavelet coefficients are shown in Figure 8c. The signatures of the Tharsis Montes, Elysium Rise and Valles Marineris can be discerned up to l_a = 64, and are associated with a central positive maximum surrounded by a circular minimum. Impact basins are resolved at various wavelet degrees depending on their size, and are characterized by negative coefficients of topography and positive coefficients of gravity anomalies, indicating mass concentrations. The Hellas basin in the southern hemisphere does not show strong gravity anomalies, whereas the Utopia basin has a large positive gravity anomaly with negative topography.

[41] Anisotropic wavelet coefficients of gravity and topography are shown in Figure 8d. The observed patterns of anisotropy exhibit similar trends to the isotropic patterns. The strongest anisotropic signals at wavelet degree 8 correspond to the Tharsis and Elysium Rise, and the Hellas basin. Beyond degree 8 the Tharsis Montes dominate both the anisotropic gravity and topography signals.

3.3.3. Wavelet Admittance and Correlation

[42] The admittance and correlation maps are shown in Figure 9a. These results confirm and extend previous observations of global admittance and correlation on Mars [*Kido et al.*, 2003; *McGovern et al.*, 2002]. Several first-order features are clearly seen on the maps: (1) regions of elevated and positive admittance and correlation are localized around volcanic constructs: Olympus Mons, the Tharsis Montes, Alba Patera, Valles Marineris, and Elysium Rise; (2) the southern highlands display consistently low admittance values and moderate to high positive correlation; (3) in contrast, the northern lowlands are characterized by large positive and negative coefficients of both admittance and correlation with significant small-scale variations; (4) the Hellas basin shows high correlation with moderate admittance; and (5) the largest mascon basins (Utopia, Isidis and Argyre) are characterized by degree-dependent admittance and correlation with negative values at wavelet degree 16, reflecting gravity highs coupled with topographic lows. We note that, with the exception of some large impact basins, the vast majority of locations displaying negative coefficients occur in the northern lowlands.

[43] Results of anisotropic coefficients of admittance and correlation are shown in Figure 9b. At wavelet degrees 16 and 32 the admittance and correlation at major volcanic edifices are isotropic. The northern lowlands show larger variations in both admittance and correlation anisotropic coefficients. At degree 16 the largest coefficients in the

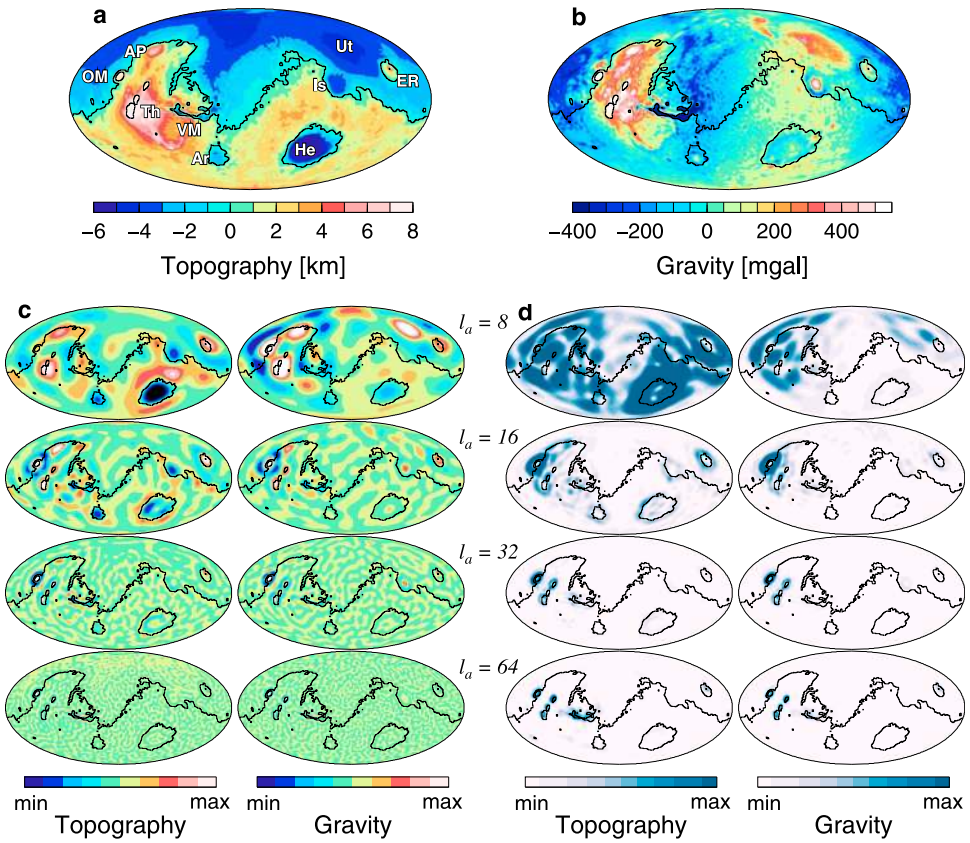

Figure 8. Same as Figure 4 but for Mars. Note how the large volcanoes dominate both the gravity and topography coefficients at all wavelet degrees, obscuring the signal elsewhere. AP, Alba Patera; Ar, Argyre; ER, Elysium Rise; He, Hellas; Is, Isidis; OM, Olympus Mons; Th, Tharsis; Ut, Utopia; VM, Valles Marineris.

correlation map are localized south of the Elysium Rise and directly East of the Tharsis Rise. At degree 32 the largest coefficients lie midway between Elysium and Olympus Mons, and to the east of Tharsis.

3.3.4. Comparison With Previous Studies

[44] The work by *Kido et al.* [2003] describes the only other known example of a spherical wavelet transform applied to the gravity and topography of Mars. Technically,

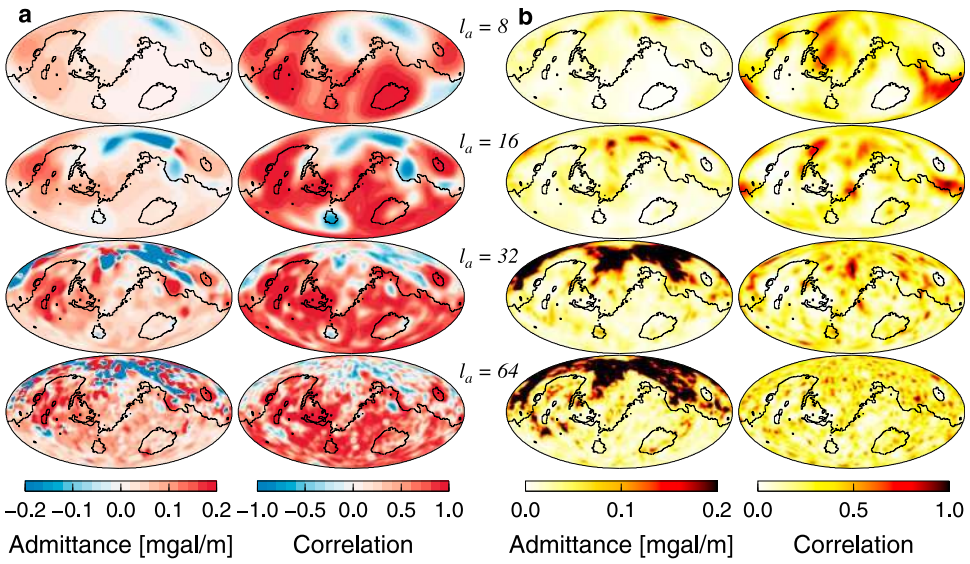

Figure 9. Same as Figure 5 but for Mars.

the transform used by *Kido et al.* [2003] is not a wavelet transform because they use a spherical correction to Euclidian wavelets that does not preserve self-similarity at different dilations. In practice they define an axisymmetric kernel based on the zeroth-order Bessel function of the first kind modulated by a localizing (Gaussian) window, which is equivalent to the azimuthal averaging of a real Morlet wavelet prior to the application of the transform. The two main differences lie in the spherical correction (we use a stereographic projection which preserves self-similarity) and the azimuthal averaging (we average the wavelet coefficients rather than the wavelet basis). We note that, although irrelevant to the comparison of results, a third difference is a significant improvement in the computational costs of the wavelet algorithm developed by *McEwen et al.* [2007a], which allows one to perform the fully directional wavelet transform on a personal computer.

[45] In the analysis of *Kido et al.* [2003] the width of the kernel is proportional to l_w/σ where l_w is the wave number on the sphere corresponding to an angular degree of the spherical harmonics (equivalent to l_a in our work) and σ controls the balance of localization. Manipulating the ratio l_w/σ is thus equivalent to varying the wavelet dilation a. Results of the isotropic wavelet coefficients (Figure 8c) should be compared with those shown in Figures 7c and 7d of *Kido et al.* [2003]; these are very similar. The admittance and correlation functions in Figures 7e and 7f of *Kido et al.* [2003] are also very close to our results (Figure 9a). Minor difference may be due to slightly different wavelet basis functions, localizing parameters, and data sets.

[46] Using the spectral localization technique of *Simons et al.* [1997], *McGovern et al.* [2002] calculated gravity-topography admittance and correlation maps of Mars by moving a spatiospectral window with a fixed width of $L_{win} = 10$, which corresponds to a maximum wavelength of $\approx$ 1200 km, over the full spherical harmonic spectrum. The fixed window approach degrades spatial resolution at the largest degrees compared to the wavelet transform, and therefore some differences are expected at small wavelengths. Despite these differences the results are qualitatively very similar and show larger positive and negative admittance and correlation anomalies in the northern hemisphere than in the south.

3.4. The Moon

3.4.1. Data

[47] Recent missions to the Moon (Lunar Reconnaissance Orbiter, SELENE) are starting to provide high-resolution topographic and gravity models of the lunar farside. Here we use gravity and topography data from the SELENE mission (Figures 10a and 10b). The topography model LALT360 was obtained from the laser altimeter instrument (updated from *Araki et al.* [2009]). The gravity model SGM100h was obtained by four-way Doppler measurements of the main orbiter by the Relay Sub-satellite Transponder (RSAT) [*Matsumoto et al.*, 2010]. These models provide dramatic improvement over previous ones, in particular on the farside of the Moon. We note, however, that data quality may differ between farside and nearside lunar gravity due to the use of a subsatellite relay.

3.4.2. Wavelet Transform

[48] Isotropic wavelet coefficients of gravity and topography are shown in Figure 10c. The largest topographic signal is the dramatic elevation difference at the northeastern rim of the South Pole–Aitken (SPA) basin observed at wavelet degree 8. Interestingly, there is little associated gravity anomaly at the same scale, indicating near-isostatic compensation. The largest gravity signals coincide with the various mascons (Imbrium, Serenitatis, Crisium, Orientale) observed mostly on the lunar nearside.

[49] Anisotropic wavelet coefficients of gravity and topography are shown in Figure 10d. Apart from the signature of the mascons, the nearside lowlands are mostly isotropic whereas the farside highlands are highly anisotropic in both gravity and topography coefficients.

3.4.3. Wavelet Admittance and Correlation

[50] The admittance and correlation maps (Figure 11a) show a remarkable dichotomy, similar to what is observed for Mars. The lowland basins display large negative admittance and correlation at wavelet degrees $l_a < 64$, whereas the farside highlands show high positive admittance and correlation, except for a few large impact basins. All large impact basins have negative values at wavelet degrees corresponding to their size. In contrast, the SPA basin shows both positive admittance and correlation at all wavelet degrees.

[51] Anisotropic wavelet coefficients of admittance and correlation are shown in Figure 11b. The observed patterns are reversed with respect to the isotropic maps and show larger anisotropy in both admittance and correlation on the nearside lowlands at all wavelet degrees, whereas the farside highlands are mostly isotropic.

4. Discussion

[52] In this section we discuss the broad implications of the observed wavelet admittance and correlation maps for the flexure of the lithosphere on each terrestrial body in a qualitative way. We first provide a basic description of the thin elastic shell model and expected observations to compare with results reported herein. For similar discussions on the flexural modeling the reader is referred to the work by *Wieczorek* [2007, and references therein].

4.1. Flexure of a Thin Elastic Shell

[53] Modeling the lithosphere as a thin elastic shell assumes that loads are in flexural isostatic equilibrium. In this model the gravity field is linearly related to the topography via a linear isostatic response function. Deconvolving the topography from the gravity (effectively calculating the admittance function) provides an estimate of this transfer function, which can then be modeled by loading the elastic shell either at a single interface by topography (surface load) or by internal mass anomalies (bottom load), or at both surface and bottom interfaces simultaneously (dual loading). The admittance function thus depends on a number of flexural parameters such as the density of the crust (ρ_c) and mantle (ρ_m), parameters of the elastic shell (Poisson's ratio (ν), Young's modulus (E) and thickness (T_e)), crustal thickness (T_c), the depth of bottom loading (z), gravitational acceleration (g), the mean planetary radius (R), and, in the case of the dual loading scenario, the load ratio (f) and load correlation (α) between the initial loads [*Wieczorek*, 2007]. Of these, the density structure and crustal and elastic thicknesses are usually the important parameters that one wishes to estimate. The depth to bottom loading, loading

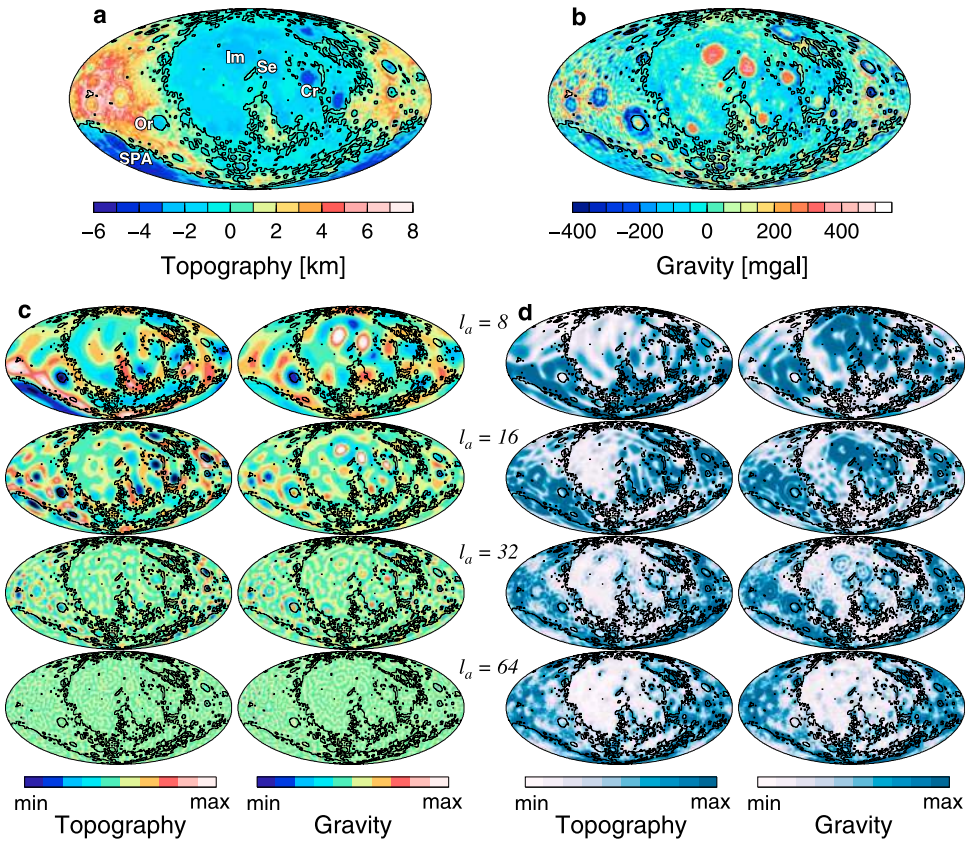

Figure 10. Same as Figure 4 but for the Moon. Cr, Crisium; Im, Imbrium; Or, Orientale; Se, Serenitatis; SPA, South Pole–Aitken.

ratio and load correlation are model parameters that are usually fixed in the inversion.

[54] Consider first a model with loading at a single interface. In this case the net deflection produced by the load mimics the shape of the load and the gravity-topography correlation, γ, is always 1. If the loads are supported locally as in the Airy isostatic model (i.e., no rigidity), then the expected gravity anomaly, and hence admittance, is small. For loads supported by bending rigidity, the admittance has an inflection point from low to high values at a given spherical harmonic degree which gives an indication of T_e. If the inflection point occurs at large degrees, we can use the

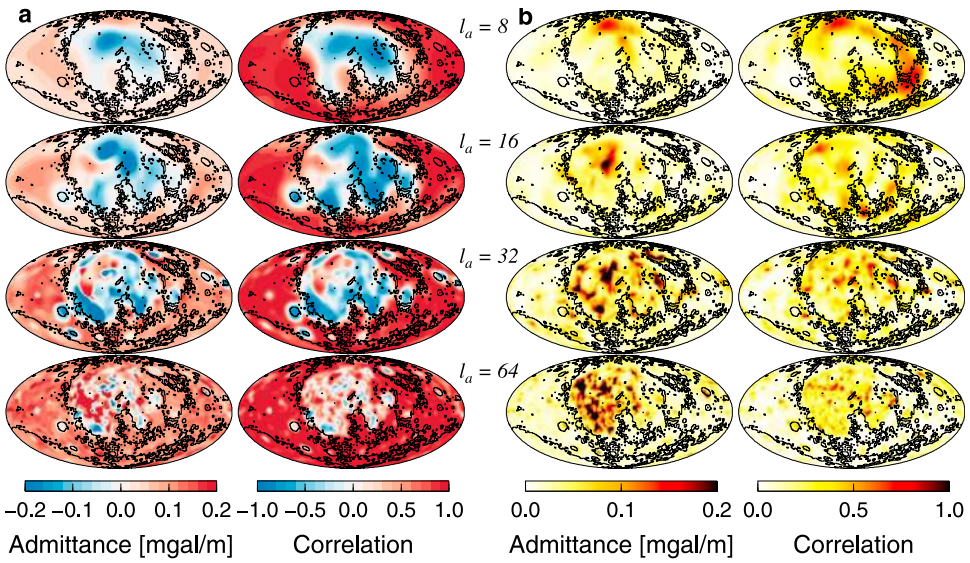

Figure 11. Same as Figure 5 but for the Moon.

Cartesian approximation for the elastic plate [e.g., *Turcotte and Schubert*, 2002],

$$\rho g \lambda_F^4 \sim E T_e^3 / 12(1-\nu^2), \quad (24)$$

where λ_F is the equivalent wavelength obtained from equation (13). Although an oversimplification of reality, this relation can be used to estimate rough bounds on T_e of the terrestrial planets. More importantly, however, this equation cannot be used to estimate T_e where the admittance or correlation is negative (e.g., mascons).

[55] In the dual loading model, one has to make further assumptions about the loading structure in order to estimate flexural parameters. If the loads are due to the same causative process (e.g., volcanoes), both surface and bottom deflections of the elastic shell are in phase and the correlation function is 1 over a large portion of the spectrum. The flexural parameters can then be estimated from the admittance by assuming a given loading ratio between surface and internal loads. A degree-dependent correlation function indicates failure of this simple model and additional assumptions regarding the loading structure are required to invert the admittance. In the example above, the load correlation, α, is also 1 because loads are in phase. One can relax this assumption by selecting a particular statistical relationship between surface and internal loads (in phase, out of phase, random phase). In such a model the isostatic functions can be negative if loads are out of phase, which is a clear diagnostic of flexural support. Indeed, any large initial loads will always flex the shell so as to bring the final flexed surfaces in phase, such that negative admittance and correlation functions at low wavelet degrees imply that loads are supported elastically.

4.2. Anisotropy

[56] Directional variations in either the admittance or correlation functions indicate that additional model parameters are required to explain the data. There is currently no thin elastic shell model that incorporates the effect of anisotropy as observed here. Since most model parameters are intrinsically isotropic, only a few modifications to the current models may be considered. A straightforward extension is to consider the loading of a thin orthotropic elastic shell (different rigidities in two perpendicular directions). In the Cartesian domain the equations for the flexure of an orthotropic plate have been successfully applied to estimate the anisotropic rigidity of the lithosphere on Earth [*Swain and Kirby*, 2003; *Kirby and Swain*, 2006]. In the spherical domain the equations may be derived in a similar fashion [e.g., *Kraus*, 1967]. Such a model can give useful estimates if the inflection point at the wavelength of flexure varies azimuthally (most likely at low wavelet degrees). Directionally dependent admittance and correlation functions at large wavelet degrees (i.e., larger than corresponding transition wavelength λ_F) cannot be modeled using an orthotropic shell model. Alternatively, the assumptions regarding the loading structure may perhaps be modified to allow for load directionality, in addition to load correlation and load ratio. The anisotropy at large degrees could also indicate localized compensation in a preferred direction due to faulting of the crust [e.g., *Simons et al.*, 2003] or the effect of sedimentation or erosion which can erase the directionality in the topographic signal while leaving the anisotropic gravity signature intact if subsurface loads are uncompensated.

4.3. Implications for the Lithosphere of the Terrestrial Planets

4.3.1. Earth

[57] Early studies of the admittance on Earth have focused on estimating the density structure of the lithosphere [*Dorman and Lewis*, 1970; *Lewis and Dorman*, 1970; *Dorman and Lewis*, 1972]. Models were further refined for the surface loading of an elastic plate [e.g., *Banks et al.*, 1977; *McNutt and Parker*, 1978]. *Forsyth* [1985] subsequently developed the Bouguer coherence (squared complex correlation between Bouguer gravity and topography) method where T_e is estimated by assuming random correlation between initial surface and subsurface loading. This assumption is valid to a certain extent due to the effects of constant load reorganization by plate tectonics, erosion and sedimentation. Since the work of *Forsyth* [1985], most studies have used the Bouguer coherence method to estimate T_e on continents. These studies show that continental interiors are much stronger, and thus thicker, than the surrounding margins and ocean basins. In addition, plate margins are shown to be strongly anisotropic with weak directions perpendicular to major boundaries and lithospheric fabric [e.g., *Simons et al.*, 2003; *Kirby and Swain*, 2006; *Audet et al.*, 2007].

[58] Alternatively, some authors have argued that the Bouguer coherence method is biased by low topography over most continental areas, and that loads with no topographic expressions will overestimate T_e [*McKenzie and Fairhead*, 1997; *McKenzie*, 2003]. These authors propose to use the admittance between free-air gravity and topography with uniform f, rather than the load deconvolution method, because these should be similar over a large range of wavelengths. These studies suggest that, in contrast to estimates obtained from the Bouguer coherence method, continents are weak and T_e is nowhere greater than the crustal thickness. Subsequently, *Kirby and Swain* [2009] have used synthetic models with various scenarios of lithospheric loading to show that both methods are biased in the presence of unexpressed loads, and that T_e >100 km can still be recovered in such cases. Nevertheless, as *Wieczorek* [2007] argues, both the admittance and correlation functions should be used simultaneously in order to obtain meaningful estimates of lithospheric parameters, which has never been attempted as yet (see *Stark et al.* [2003] for an alternative approach).

[59] Regardless of the loading scenario, we can still gain useful information on lithospheric structure from the global admittance and correlation maps (Figure 5). The larger admittance values in the continents with increasing wavelet degrees implies a larger mass anomaly per unit topography. If we assume a uniform crustal density, the larger admittance on continents indicates that the extra mass must be supported mechanically. The transition from compensated to supported topography (low to high admittance) occurs at wavelet degrees l_a< 64 for most continental areas, corresponding roughly to λ_F > 625 km (equation (13)). Taking values typical for the Earth (E = 100 GPa, ν = 0.25, ρ_c = 2800 kg/m^3, g = 9.8 m/s^2) and using equation (24), this corresponds roughly to T_e > 75 km. Such values, although

perhaps unrealistically large due to the assumption of surface loading only in equation (24), are more consistent with results obtained with the Bouguer coherence method. We note, however, that a formal inversion of wavelet admittance and correlation for T_e using both planar and spherical wavelet transforms is needed to assess how much of these differences can be attributed to the effect of neglecting Earth curvature in the planar method. Based on the patterns of transitional admittance it appears that the lithosphere of Eurasia and Africa are strongest. We note that the anisotropic admittance pattern follows closely that of the isotropic admittance (Figure 5), which supports the preliminary conclusions.

4.3.2. Venus

[60] Estimates of T_e on Venus have been obtained using gravity and topography by, e.g., *Johnson and Sandwell* [1994], *Simons et al.* [1997], *Barnett et al.* [2000], *Hoogenboom et al.* [2005], and *Anderson and Smrekar* [2006]. The study by *Anderson and Smrekar* [2006] estimated T_e from a global mapping of the admittance function using the spatiospectral localization technique of *Simons et al.* [1997] and a dual loading model, and found T_e varying between 0 and 100 km with approximately 50% of the planet having $T_e < 20$ km. Because data accuracy is lower than that of other planets, our analysis is only valid to wavelet degrees $l_a \leq 32$. Unfortunately, as shown by *Anderson and Smrekar* [2006], most admittance curves have their inflection point at around degree 60. Nevertheless, we can still estimate upper bounds on T_e from the remaining wavelet degrees analyzed.

[61] The high positive correlation indicates either that a simple surface loading model, or a dual loading model with correlated initial loads, is valid. High positive correlation and high admittance at low wavelet degrees ($l_a < 16$) may be explained by dynamic topography caused by mantle convection [*McKenzie*, 1994]. The lower admittance at the Aphrodite and Ishtar Terrae suggests near-complete compensation, consistent with the low T_e values reported by *Anderson and Smrekar* [2006]. Taking values estimated for Venus (ρ_c = 2800 kg/m^3, g = 9.8 m/s^2), and evaluating a transitional admittance at wavelet degree $l_a > 64$, we obtain an upper bound of $T_e < 70$ km. The absence of admittance and/or correlation anisotropy on Venus may suggest that the lithosphere does not record significant fabric from dynamic processes operating within the planet. Alternatively, it may indicate that such processes produce isotropic loads such as coronae that are associated with transient plume-like upwellings [*Johnson and Richards*, 2003]. Finally, we note that the uniformly high positive correlation at wavelet degree 8 is atypical of the terrestrial planets analyzed herein, and indicates that the sublithospheric mantle of Venus is more homogeneous compared to Earth's mantle, in agreement with previous findings [*Phillips and Lambeck*, 1980].

4.3.3. Mars

[62] For Mars, most recent studies focus on locations that exhibit high gravity-topography correlation over a range of spherical harmonic degrees [*McGovern et al.*, 2002; *Belleguic et al.*, 2005]. As explained in section 4.1, this choice validates the use of a dual loading model with a fixed load ratio and in-phase loading to estimate flexural parameters. Because these studies are limited to a small number of locations, mostly around volcanic edifices, the estimated flexural parameters may not be representative of the true distribution. In particular, the negative admittance and correlation at low wavelet degrees ($l_a \leq 16$) in the northern hemisphere suggests that large loads are uncompensated, indicating support by a strong lithosphere. However, most of the northern lowland topography is flat and covered by a thick sediment blanket, which acts to reduce the power spectrum of topography while keeping the gravity structure relatively intact. Very small differences in the initial load correlation can thus be amplified by low-power topography to produce the large polarity swings observed in the admittance. Sedimentation could also help to explain the large anisotropic coefficients of the admittance in the northern hemisphere. A thick, flexurally supported sediment cover would erase anisotropic signals initially present in the topography, such that the ratio between a directional gravity field with an isotropic, low-power topography can produce strong heterogeneous anisotropic admittance. The fact that regions showing strong admittance anisotropy do not have correspondingly high correlation anisotropy supports this interpretation.

[63] On the other hand, strong gravity signals at low wavelet degrees in the northern versus the southern hemisphere combined with a large crustal dichotomy argues for the excavation of the crust by a very large impact basin [*Andrews-Hanna et al.*, 2008; *Marinova et al.*, 2008; *Nimmo et al.*, 2008]. This interpretation is also supported by the similarities in the admittance and correlation between the northern lowlands and large mascon basins (Argyre and Isidis), which suggests a strong Martian lithosphere. Interestingly, the strong anisotropy at low wavelet degrees ($l_a \leq 16$) in the correlation appears in regions of both low admittance and low admittance anisotropy. These regions do not coincide with any known surface feature, and may indicate flexural support by an orthotropic elastic shell. Alternatively, as *Wieczorek* [2007] points out, the degree-dependent correlation function is affected by gravitational "noise" that is uncorrelated with the topography, which may be responsible for some of the features observed in the correlation maps [see also *McKenzie*, 2003].

[64] Finally, T_e on Mars may vary by as much as 1 order of magnitude ($10 < T_e < 160$ km) [*McGovern et al.*, 2002], as observed in the significant variations in the transition wavelength. These bounds are only approximately valid for the Martian highland regions where admittance and correlation are positive.

4.3.4. The Moon

[65] Few studies have focused on estimating T_e on the Moon. Early studies include that by *Solomon and Head* [1980], who used mapped features around impact craters to calculate T_e, and *Arkani-Hamed* [1998] who investigated the flexural support of mascons using gravity and topography data from the Clementine mission. More recently, *Crosby and McKenzie* [2005] used line of sight acceleration data of the lunar nearside from the Lunar Prospector mission to estimate the admittance and coherence, which were then modeled to obtain T_e. Most studies find T_e on the order of a few tens of km. To our knowledge, this is the first study of gravity-topography admittance to use the newest high-resolution data sets with complete coverage of the farside gravity field.

[66] Perhaps the most spectacular feature of the Moon's admittance and correlation maps is the large contrast between the farside and the nearside. The dichotomy is characterized

by large negative and anisotropic admittance and correlation coefficients on the nearside and positive isotropic coefficients on the farside. The origin of the anisotropy is enigmatic as both topography and gravity coefficients show the opposite trend: isotropy on the nearside and anisotropy on the farside. The smooth and negative topography of the nearside is characterized by lavas enriched in incompatible elements (KREEP terrane), which implies remelting of the lunar floor, possibly due to higher concentration of radiogenic elements in the crust [*Wieczorek et al.*, 2006]. In addition, tectonic landforms occur predominantly on the lunar nearside [*Watters and Johnson*, 2010]. The stronger anisotropy could then represent fabric originating from various landforms such as wrinkle ridges and rilles. Regardless of its origin, the nearside admittance and correlation anisotropy suggests a strong nearside lithosphere.

[67] The origin of the dichotomy is a matter of much debate [*Wieczorek et al.*, 2006]. The similarity in structure between the Moon and Mars may provide clues on the evolution of the lithosphere of these bodies. These are characterized by hemispherical contrasts in admittance and correlation coefficients, where the signature of lowlands is similar to that of large mascons. This dichotomy also coincides with large differences in crustal structure [*Wieczorek and Zuber*, 2004; *Wieczorek and Phillips*, 1998], reinforcing the idea that large contrasts in lithospheric rigidity exist on both bodies. In each case the lowlands, which have been resurfaced by laval flows, are presumably underlain by strong lithosphere; in contrast, the pristine rocks of both lunar and Martian highlands are supported by weaker lithosphere. As is widely recognized, the two largest identified impact basins in the solar system (apart from the postulated Borealis basin on Mars), South Polar–Aitken on the Moon and Hellas on Mars, have signatures that indicate near-complete compensation of impact-induced loads. Why these impact events did not produce associated mascons is enigmatic; however the fact that they are located in highland regions supports the interpretation of weak underlying lithosphere.

[68] Finally, assuming crustal density of 2900 kg/m^3 [*Wieczorek et al.*, 2006], the transition in admittance at low wavelet degrees ($l_a \sim 16$) suggests $T_e \sim 50$ km in highlands where admittance and correlation are positive (thus excluding mascons), in agreement with previous studies [*Arkani-Hamed*, 1998].

5. Conclusion

[69] In this paper we describe the application of a spherical wavelet analysis using directional and isotropic wavelets constructed from the azimuthal averaging of directionally adjacent Morlet wavelets. The algorithm is used to calculate the isotropic and anisotropic wavelet coefficients of topography and gravity of the terrestrial planets and their cross-spectral quantities (admittance and correlation). The results are compared with the published literature and reveal interesting features that have implications for the flexural support of planetary lithospheres.

[70] On Earth, low admittance and high correlation at long wavelengths indicates compensation of lithospheric loads. The increase in admittance on continents suggests that T_e is likely much higher compared to ocean basins, with values ranging roughly between 75 and 200 km. The origin of the anisotropy of Earth's continental lithosphere is difficult to determine from such global maps and further study is warranted. On Venus, the admittance and correlation maps show uniformly low positive and isotropic values, possibly reflecting the combination of isostatic compensation and dynamic topography due to convection. The various high-elevation terrains display lower admittance than the low-lying plains, indicating weaker lithosphere. The high correlation at low wavelet degrees likely implies a homogeneous sublithospheric mantle. On Mars, the admittance and correlation maps are characterized by the dichotomy between northern lowlands, where admittance and correlation are negative and highly anisotropic, and the southern highlands, where admittance is low and correlation is high. Large mascons (Isidis and Argyre) also display negative admittance and correlation reflecting flexural support, whereas the Hellas basin is isostatically compensated. The various Martian volcanic provinces show both high admittance and correlation with little anisotropy, indicating high-density loads. Similar to Mars, the Moon is characterized by a strong hemispherical dichotomy where the nearside lowlands exhibit negative and highly anisotropic admittance and correlation, whereas the farside highlands show isotropic, positive low admittance and high correlation. Large lunar mascons are characterized by negative values, whereas the South Pole–Aitken basin is fully compensated.

[71] Results from this paper are preliminary, and only serve to illustrate a useful application of the spherical wavelet technique. Formal inversions of the admittance and correlation maps will be necessary to elucidate the nature of the differences in lithospheric structure between these planetary bodies.

[72] Finally, the wavelet analysis presented herein can be similarly applied to any planetary body in the solar system with sufficiently high resolution data. Its use is not restricted to gravity and topography, however, and one can find potential applications in the study of planetary magnetic fields, etc. With the upcoming release of data from different interplanetary missions (e.g., Lunar Reconnaissance Orbiter, MESSENGER), such a wavelet analysis will certainly prove to be a useful tool for the rapid interpretation and dissemination of results.

[73] **Acknowledgments.** The software FastCSWT (http://www.mrao.cam.ac.uk/~jdm57/) was used to perform the wavelet transform calculations. The softwares SHTOOLS (http://www.ipgp.fr/~wieczor/SHTOOLS/SHTOOLS.html) and HEALPix (http://healpix.jpl.nasa.gov/) were used to process the data products obtained from the Planetary Data System Geoscience Node archives (http://pds-geosciences.wustl.edu/default.htm). The lunar data were obtained from the SELENE data archive (https://www.soac.selene.isas.jaxa.jp/archive/index.html.en). This work is supported by the Miller Institute for Basic Research in Science (UC Berkeley). The author acknowledges discussions with M. Manga, M. Jellinek, and C. Johnson. This paper was much improved by constructive comments from the Associate Editor and two anonymous reviewers.

References

Amante, C., and B. W. Eakins (2009), ETOPO1 1 arc-minute global relief model: Procedures, data sources and analysis, *Tech. Memo. 24*, 19 pp., NOAA, Boulder, Colo.

Anderson, F. S., and S. E. Smrekar (2006), Global mapping of crustal and lithospheric thickness on Venus, *J. Geophys. Res.*, *111*, E08006, doi:10.1029/2004JE002395.

Andrews-Hanna, J. C., M. R. Zuber, and W. B. Banerdt (2008), The Borealis basin and the origin of the Martian crustal dichotomy, *Nature*, *453*, 1212–1215.

Antoine, J.-P., and P. Vandergheynst (1999), Wavelets on the 2-sphere: A group-theoretical approach, *Appl. Comput. Harmon. Anal.*, *7*, 262–291.
Antoine, J.-P., R. Murenzi, and P. Vandergheynst (2004), *Two-Dimensional Wavelets and Their Relatives*, Cambridge Univ. Press, Cambridge, U. K.
Araki, H., et al. (2009), Lunar global shape and polar topography derived from Kaguya-LALT laser altimetry, *Science*, *323*, 897–900.
Arkani-Hamed, J. (1998), The lunar mascons revisited, *J. Geophys. Res.*, *103*, 3709–3739.
Arkani-Hamed, J. (2000), Strength of Martian lithosphere beneath large volcanoes, *J. Geophys. Res.*, *105*, 23,197–23,207.
Audet, P., and J.-C. Mareschal (2007), Wavelet analysis of the coherence between Bouguer gravity and topography: Application to the elastic thickness anisotropy in the Canadian Shield, *Geophys. J. Int.*, *168*, 287–298.
Audet, P., A. M. Jellinek, and H. Uno (2007), Mechanical controls on the deformation of continents at convergent margins, *Earth Planet. Sci. Lett.*, *264*, 151–166, doi:10.1016/j.epsl.2007.09.024.
Banks, R. J., R. L. Parker, and S. P. Huestis (1977), Isostatic compensation on a continental scale: Local versus regional mechanisms, *Geophys. J. R. Astron. Soc.*, *51*, 431–452.
Barnett, D. N., F. Nimmo, and C. McKenzie (2000), Elastic thickness estimates for Venus using line of sight accelerations from Magellan Cycle 5, *Icarus*, *146*, 404–419.
Belleguic, V., P. Lognonné, and M. A. Wieczorek (2005), Constraints on the Martian lithosphere from gravity and topography data, *J. Geophys. Res.*, *110*, E11005, doi:10.1029/2005JE002437.
Crosby, A. G., and D. McKenzie (2005), Measurements of the elastic thickness under ancient lunar terrain, *Icarus*, *173*, 100–107.
Dorman, L. M., and B. T. R. Lewis (1970), Experimental isostasy: 1. Theory of the determination of the Earth's isostatic response to a concentrated load, *J. Geophys. Res.*, *75*, 3357–3365.
Dorman, L. M., and B. T. R. Lewis (1972), Experimental isostasy: 3. Inversion of the isostatic green function and lateral density changes, *J. Geophys. Res.*, *77*, 3068–3077.
Forsyth, D. W. (1985), Subsurface loading and estimates of the flexural rigidity of continental lithosphere, *J. Geophys. Res.*, *90*, 12,623–12,632.
Górski, K. M., E. Hivon, A. J. Banday, B. D. Wandelt, F. K. Hansen, M. Reinecke, and M. Bartelmann (2005), Healpix—A framework for high resolution discretization and fast analysis of data distributed on the sphere, *Astrophys. J.*, *622*, 759–771.
Hoogenboom, T., G. Houseman, and P. Martin (2005), Elastic thickness estimates for coronae associated with chasmata on Venus, *J. Geophys. Res.*, *110*, E09003, doi:10.1029/2004JE002394.
Johnson, C. L., and M. A. Richards (2003), A conceptual model for the relationship between coronae and large-scale mantle dynamics on Venus, *J. Geophys. Res.*, *108*(E6), 5058, doi:10.1029/2002JE001962.
Johnson, C. L., and D. T. Sandwell (1994), Lithospheric flexure on Venus, *Geophys. J. Int.*, *119*, 627–647.
Kido, M., D. A. Yuen, and A. P. Vincent (2003), Continuous wavelet-like filter for a spherical surface and its application to localized admittance function on Mars, *Phys. Earth Planet. Inter.*, *135*, 1–14.
Kirby, J. F. (2005), Which wavelet best reproduces the Fourier power spectrum?, *Comput. Geosci.*, *31*, 846–864.
Kirby, J. F., and C. J. Swain (2006), Mapping the mechanical anisotropy of the lithosphere using a 2-D wavelet coherence, and its application to Australia, *Phys. Earth Planet. Int.*, *158*, 122–138.
Kirby, J. F., and C. J. Swain (2009), A reassessment of spectral T_e estimation in continental interiors: The case of North America, *J. Geophys. Res.*, *114*, B08401, doi:10.1029/2009JB006356.
Kraus, H. (1967), *Thin Elastic Shells*, John Wiley, New York.
Lewis, B. T. R., and L. M. Dorman (1970), Experimental isostasy: 2. An isostatic model for the U.S.A. derived from gravity and topographic data, *J. Geophys. Res.*, *75*, 3367–3386.
Lowry, A. R., and R. B. Smith (1994), Flexural rigidity of the Basin and Range-Colorado Plateau-Rocky Mountain transition from coherence analysis of gravity and topography, *J. Geophys. Res.*, *99*, 20,123–20,140.
Lowry, A. R., and R. B. Smith (1995), Strength and rheology of the western U.S. Cordillera, *J. Geophys. Res.*, *100*, 17,947–17,963.
Marinova, M. M., O. Aharonson, and E. Asphaug (2008), Mega-impact formation of the Mars hemispheric dichotomy, *Nature*, *452*, 1216–1219.
Matsumoto, K., et al. (2010), An improved lunar gravity field model from SELENE and historical tracking data: Revealing the farside gravity features, *J. Geophys. Res.*, *115*, E06007, doi:10.1029/2009JE003499.
McEwen, J. D., M. P. Hobson, A. N. Lasenby, and D. J. Mortlock (2005), A high-significance detection of non-Gaussianity in the WMAP 1-year data using directional spherical wavelets, *Mon. Not. R. Astron. Soc.*, *359*, 1583–1596.
McEwen, J. D., M. P. Hobson, D. J. Mortlock, and A. N. Lasenby (2007a), Fast directional continuous spherical wavelet transform algorithms, *IEEE Trans. Signal Process.*, *55*(2), 520–529.
McEwen, J. D., P. Vielva, M. P. Hobson, E. Martínez-González, and A. N. Lasenby (2007b), Detection of the ISW effect and corresponding dark energy constraints made with directional spherical wavelets, *Mon. Not. R. Astron. Soc.*, *376*, 1211–1226.
McGovern, P. J., S. C. Solomon, D. E. Smith, M. T. Zuber, M. Simons, M. A. Wieczorek, R. J. Philips, G. A. Neumann, O. Aharonson, and J. W. Head (2002), Localized gravity/topography admittance and correlation spectra on Mars: Implications for regional and global evolution, *J. Geophys. Res.*, *107*(E12), 5136, doi:10.1029/2002JE001854. (Correction, *J. Geophys. Res.*, 109, E07007, doi:10.1029/2004JE002286, 2004.)
McKenzie, D. (1994), Relationship between topography and gravity on Earth and Venus, *Icarus*, *112*, 55–88.
McKenzie, D. (2003), Estimating T_e in the presence of internal loads, *J. Geophys. Res.*, *108*(B9), 2438, doi:10.1029/2002JB001766.
McKenzie, D. P., and J. D. Fairhead (1997), Estimates of the effective elastic thickness of the continental lithosphere from Bouguer and free air gravity anomalies, *J. Geophys. Res.*, *102*, 27,523–27,552.
McKenzie, D. P., D. N. Barnett, and D.-N. Yuan (2002), The relationship between Martian gravity and topography, *Earth Planet. Sci. Lett.*, *195*, 1–16.
McNutt, M. K., and R. L. Parker (1978), Isostasy in Australia and the evolution of the compensation mechanism, *Science*, *199*, 773–775.
Nimmo, F., S. D. Hart, D. G. Korycansky, and C. B. Agnor (2008), Implications of an impact origin for the Martian hemispheric dichotomy, *Nature*, *452*, 1220–1223.
Pérez-Gussinyé, M., A. R. Lowry, A. B. Watts, and I. Velicogna (2004), On the recovery of effective elastic thickness using spectral methods: Examples from synthetic data and from the Fennoscandian Shield, *J. Geophys. Res.*, *109*, B10409, doi:10.1029/2003JB002788.
Phillips, R. J., and K. Lambeck (1980), Gravity fields of the terrestrial planets: Long-wavelength anomalies and tectonics, *Rev. Geophys.*, *18*, 27–76.
Sandwell, D. T., and W. H. F. Smith (1997), Marine gravity anomaly from Geosat and ERS 1 satellite altimetry, *J. Geophys. Res.*, *102*, 10,039–10,054.
Simons, F. J., M. T. Zuber, and J. Korenaga (2000), Isostatic response of the Australian lithosphere: Estimation of effective elastic thickness and anisotropy using multitaper spectral analysis, *J. Geophys. Res.*, *105*, 19,163–19,184.
Simons, F. J., R. D. van der Hilst, and M. T. Zuber (2003), Spatiospectral localization of isostatic coherence anisotropy in Australia and its relation to seismic anisotropy: Implications for lithospheric deformation, *J. Geophys. Res.*, *108*(B5), 2250, doi:10.1029/2001JB000704.
Simons, F. J., F. A. Dahlen, and M. A. Wieczorek (2006), Spatiospectral concentration on a sphere, *SIAM Rev.*, *48*, 504–536, doi:10.1137/S0036144504445765.
Simons, M., and B. H. Hager (1997), Localization of the gravity field and the signature of glacial rebound, *Nature*, *390*, 500–504.
Simons, M., S. C. Solomon, and B. H. Hager (1997), Localization of gravity and topography: Constraints on the tectonics and mantle dynamics of Venus, *Geophys. J. Int.*, *131*, 24–44.
Smith, D. E., W. L. Sjogren, G. L. Tyler, G. Balmino, F. G. Lemoine, and A. S. Konopliv (1999a), The gravity field of Mars: Results from Mars Global Surveyor, *Science*, *286*, 94–97.
Smith, D. E., et al. (1999b), The global topography of Mars and implications for surface evolution, *Science*, *284*, 1495–1503.
Smith, W. H. F., and D. T. Sandwell (1997), Global sea floor topography from satellite altimetry and ship depth soundings, *Science*, *277*, 1956–1962.
Solomon, S. C., and J. W. Head (1980), Lunar mascons basins: Lava infilling, tectonics, and evolution of the lithosphere, *Rev. Geophys.*, *18*, 107–141.
Solomon, S. C., and J. W. Head (1990), Heterogeneities in the thickness of the elastic lithosphere of Mars: Constraints on heat flow and internal dynamics, *J. Geophys. Res.*, *95*, 11,073–11,083.
Spasojevic, S., M. Gurnis, and R. Sutherland (2010), Mantle upwellings above slab graveyards linked to the global geoid lows, *Nat. Geosci.*, *3*, 435–438.
Stark, C. P., J. Stewart, and C. J. Ebinger (2003), Wavelet transform mapping of effective elastic thickness and plate loading: Validation using synthetic data and application to the study of southern African tectonics, *J. Geophys. Res.*, *108*(B12), 2558, doi:10.1029/2001JB000609.
Swain, C. J., and J. F. Kirby (2003), The coherence method using a thin anisotropic plate model, *Geophys. Res. Lett.*, *30*(19), 2014, doi:10.1029/2003GL018350.
Turcotte, D. L., and G. Schubert (2002), *Geodynamics*, Cambridge Univ. Press, Cambridge, U. K.

Turcotte, D. L., R. J. Willemann, W. F. Haxby, and J. Norberry (1981), Role of membrane stresses in the support of planetary topography, *J. Geophys. Res.*, *86*, 3951–3959.

Watters, T. R., and C. L. Johnson (2010), Lunar tectonics, in *Planetary Tectonics*, edited by T. R. Watters and R. A. Schultz, pp. 121–182, Cambridge Univ. Press, Cambridge, U. K.

Wiaux, Y., L. Jacques, and P. Vandergheynst (2005), Correspondence principle between spherical and Euclidean wavelets, *Astrophys. J.*, *632*, 15–28.

Wieczorek, M. A. (2007), Gravity and topography of the terrestrial planets, in *Treatise on Geophysics*, vol. 6, *Crust and Lithosphere Dynamics*, edited by G. Schubert, pp. 165–206, Elsevier, Amsterdam.

Wieczorek, M. A., and R. J. Phillips (1998), Potential anomalies on a sphere: Applications to the thickness of the lunar crust, *J. Geophys. Res.*, *103*, 1715–1724.

Wieczorek, M. A., and F. J. Simons (2005), Localized spectral analysis on the sphere, *Geophys. J. Int.*, *162*, 655–675, doi:10.1111/j.1365-246X.2005.02687.x.

Wieczorek, M. A., and M. T. Zuber (2004), Thickness of the Martian crust: Improved constraints from geoid-to-topography ratios, *J. Geophys. Res.*, *109*, E01009, doi:10.1029/2003JE002153.

Wieczorek, M. A., et al. (2006), The constitution and structure of the lunar interior, *Rev. Mineral. Geochem.*, *60*, 221–364.

Zuber, M. T., et al. (2000), Internal structure and early thermal evolution of Mars from Mars Global Surveyor topography and gravity, *Science*, *287*, 1788–1793.

P. Audet, Department of Earth and Planetary Science, University of California, 377 McCone Hall, Berkeley, CA 94720, USA. (paudet@berkeley.edu)